Key Points:
- Electron outflow jet of asymmetric magnetic reconnection is observed
- Electron jet is unstable to Buneman-type instability generating intense electrostatic waves
- The instability leads to thermalization and braking of the electron jet

Correspondence to:
Y. V. Khotyaintsev,
yuri@irfu.se

Electron jet of asymmetric reconnection

Yu. V. Khotyaintsev[1], D. B. Graham[1], C. Norgren[1,2], E. Eriksson[1,2], W. Li[1], A. Johlander[1], A. Vaivads[1], M. André[1], P. L. Pritchett[3], A. Retinò[4], T. D. Phan[5], R. E. Ergun[6], K. Goodrich[6], P.-A. Lindqvist[7], G. T. Marklund[7], O. Le Contel[4], F. Plaschke[8], W. Magnes[8], R. J. Strangeway[9], C. T. Russell[9], H. Vaith[10], M. R. Argall[10], C. A. Kletzing[11], R. Nakamura[8], R. B. Torbert[10], W. R. Paterson[12], D. J. Gershman[12,13], J. C. Dorelli[12], L. A. Avanov[12], B. Lavraud[14], Y. Saito[15], B. L. Giles[12], C. J. Pollock[12], D. L. Turner[16], J. D. Blake[16], J. F. Fennell[16], A. Jaynes[6], B. H. Mauk[17], and J. L. Burch[18]

[1]Swedish Institute of Space Physics, Uppsala, Sweden, [2]Department of Physics and Astronomy, Uppsala University, Uppsala, Sweden, [3]Department of Physics and Astronomy, University of California, Los Angeles, California, USA, [4]LPP, CNRS, Palaiseau, France, [5]Space Science Laboratory, University of California, Berkeley, California, USA, [6]Laboratory of Atmospheric and Space Physics, University of Colorado Boulder, Boulder, Colorado, USA, [7]KTH Royal Institute of Technology, Stockholm, Sweden, [8]Space Research Institute, Austrian Academy of Sciences, Graz, Austria, [9]Department of Earth and Space Sciences, University of California, Los Angeles, California, USA, [10]Space Science Center, University of New Hampshire, Durham, New Hampshire, USA, [11]Department of Physics and Astronomy, University of Iowa, Iowa City, Iowa, USA, [12]NASA Goddard Space Flight Center, Greenbelt, Maryland, USA, [13]Department of Astronomy, University of Maryland, College Park, Maryland, USA, [14]IRAP, CNRS, Toulouse, France, [15]JAXA, Chofu, Japan, [16]Space Sciences Department, The Aerospace Corporation, El Segundo, California, USA, [17]The Johns Hopkins University Applied Physics Laboratory, Laurel, Maryland, USA, [18]Southwest Research Institute, San Antonio, Texas, USA

Abstract We present Magnetospheric Multiscale observations of an electron-scale current sheet and electron outflow jet for asymmetric reconnection with guide field at the subsolar magnetopause. The electron jet observed within the reconnection region has an electron Mach number of 0.35 and is associated with electron agyrotropy. The jet is unstable to an electrostatic instability which generates intense waves with $E_\parallel$ amplitudes reaching up to 300 mV m^{-1} and potentials up to 20% of the electron thermal energy. We see evidence of interaction between the waves and the electron beam, leading to quick thermalization of the beam and stabilization of the instability. The wave phase speed is comparable to the ion thermal speed, suggesting that the instability is of Buneman type, and therefore introduces electron-ion drag and leads to braking of the electron flow. Our observations demonstrate that electrostatic turbulence plays an important role in the electron-scale physics of asymmetric reconnection.

1. Introduction

Magnetic reconnection is a fundamental process whereby microscopic plasma processes cause macroscopic changes in magnetic field topology, so that initially separated plasmas become magnetically connected. Reconnection is asymmetric when the properties of the two reconnecting plasmas are different. Reconnection under asymmetric conditions, as well as in presence of a guide field, is the most general case which can possibly occur in astrophysical plasmas. For example, in the solar corona and chromosphere reconnection between the preexisting and emerging flux will generally be asymmetric [*Murphy et al.*, 2012]. Reconnection at Earth's magnetopause is nearly always asymmetric, typically characterized by a large change in plasma density and temperature, as well as magnetic field strength [*Khotyaintsev et al.*, 2006]. Even the otherwise symmetric magnetotail reconnection can be asymmetric under some circumstances [*Øieroset et al.*, 2004].

The presence of asymmetries and a guide field modify the structure of the reconnection region and can make it substantially different from the symmetric configuration with zero guide field. In particular, the quadrupolar Hall magnetic field structure can become bipolar [*Tanaka et al.*, 2008; *Pritchett*, 2008], and the X line and stagnation point are no longer colocated [*Cassak and Shay*, 2007]. Diamagnetic drifts in an asymmetric current layer cause the X line to drift [*Swisdak et al.*, 2003]. Electron trapping becomes asymmetric [*Egedal et al.*, 2011; *Graham et al.*, 2014], primarily occurring on the lower density side of the X line. Drift turbulence, in particular the lower hybrid drift instability (LHDI), develops at gradients leading to broadening of the current layer [*Vaivads et al.*, 2004; *Roytershteyn et al.*, 2012]. In the case of a large temperature asymmetry, reconnection enables mixing of plasmas from the two sides of the layer creating complicated electron distributions unstable

to a wide range of kinetic instabilities (streaming, temperature anisotropy, and loss cone) [*Retinò et al.*, 2006; *Viberg et al.*, 2013; *Graham et al.*, 2015, 2016a, 2016b]. Electrostatic instabilities were suggested to play an important role in the diffusion region leading to broadening of the current layer [*Jara-Almonte et al.*, 2014] and establishing an electron-ion drag [*Drake et al.*, 2003; *Che et al.*, 2010]. Whether such instabilities are essential for reconnection physics still needs to be confirmed by observations. In comparison to earlier missions such as Cluster, the Magnetospheric Multiscale (MMS) mission [*Burch et al.*, 2015] provides greatly improved particle measurements and the spacecraft separations are small, enabling multipoint observations of electron-scale processes [*Burch et al.*, 2016]. Here we investigate the detailed structure of electromagnetic fields and particle distributions in the diffusion region of asymmetric reconnection at the magnetopause using high-resolution MMS data, with particular focus on electron scales and electron dynamics.

2. Observations

We present MMS observations at Earth's magnetopause on 6 December 2015. The four MMS spacecraft were located at [8.5, −4.0, −0.6] Earth radii in geocentric solar ecliptic (GSE) coordinates, and the spacecraft were in a tetrahedron formation with ~10 km separation. We use FIELDS EDP [*Lindqvist et al.*, 2014; *Ergun et al.*, 2014], FGM [*Russell et al.*, 2014], and SCM [*Le Contel et al.*, 2014] data for electric and magnetic fields, as well as EDI [*Torbert et al.*, 2015], FPI [*Pollock et al.*, 2016], and FEEPS [*Blake et al.*, 2015] data for particles.

Figure 1 shows an overview of the magnetopause crossing at 23:38:30 UT. Owing to the small separation, data from the four spacecraft are very similar, and thus, we show data primarily from MMS4. The spacecraft are initially located in the magnetosheath (MSH) characterized by dense and relatively cold ions and electrons (Figures 1e and 1g). On the opposite side of the boundary the plasma density is ~10 times lower, and a more energetic plasma sheet (PLS) electron population (~10 keV) is present. The magnetopause (MP) is seen in the large change of B_z GSE (Figure 1a), which is changing from −30 nT in the MSH to +60 nT in the magnetosphere (MSP). Figures 1c and 1d show the ion and electron velocities. An ion jet reaching $V_z \sim -200$ km s^{-1}, seen primarily in the z component, is located at the B_z change. There is a localized density increase associated with the jet. Such a jet indicates ongoing reconnection and that the spacecraft are located southward of the reconnection X line. At the same time a very narrow and fast electron jet $V_z \sim -2000$ km s^{-1} is seen close to the peak of the ion jet. At the peak of the electron jet we see a localized signature in the electric field $E \sim 300$ mV m^{-1} (Figure 1h), corresponding to a broadband spectrum between 0.2 and 2 kHz (Figure 1i). This structure is electrostatic, as no corresponding signature can be found in the magnetic field spectrum (Figure 1j). This narrow electron jet and associated electric field signature is the primary object of this study.

We identify the MSH boundary of the reconnection layer (MSH separatrix) just after 23:38:29 UT, where the rotation in **B** starts, density starts to decrease, and electron velocity, as well as the mean electron energy, increases. There is also a substantial increase in wave activity. We identify the MSP boundary of the layer (electron edge) at 23:38:33.5 UT, where the energetic PLS population starts to decrease toward the magnetopause (Figures 1f and 1g). We discuss the electron data in detail later. Overall, it takes 4 s to cross the layer. Multispacecraft timing analysis of B_z results in a boundary velocity of $V_n = 38 \times [0.87, -0.44, -0.24]$ km s^{-1} (GSE). Most of the current (from the multispacecraft curlometer method [*Dunlop et al.*, 1988]) is localized in a 2 s long interval starting at 23:38:29.5 UT, which corresponds to a thickness of ~80 km ~ 1.5 d_i, where $d_i = c/\omega_{pi}$ is the ion inertial length in the MSH. This also corresponds to a Harris current profile $B_z = \tanh(2x/L)$, with thickness $L \simeq 1 d_i$. Thus, we observe a kinetic-scale current sheet (CS) and ion jet. Obviously, the fast electron jet has a scale well below d_i.

In order to establish the local coordinate system of the boundary, we perform minimum variance analysis (MVA) on **B**, which yields **L** = [0.02, −0.51, 0.86], **N** = [0.82, −0.48, −0.30] (GSE), and **M** = **L** × **N**. We note that the normal direction is consistent with the one obtained from timing **B** data in the LNM system shown in Figure 2a. B_N is ~3 nT at $B_L \sim 0$. Such positive B_N is consistent with the spacecraft being southward of the X line. We see that B_M is positive throughout the event, with values ~10 nT outside the CS, which corresponds to a guide field of ~20%. Within the CS B_M is enhanced, resulting in an increase of |**B**|. This feature is consistent with the dipolar Hall magnetic field expected for asymmetric guide field reconnection [*Pritchett and Mozer*, 2009], in contrast to the quadrupolar structure of symmetric reconnection.

The parallel and perpendicular electron temperatures, $T_{e\parallel}$ and $T_{e\perp}$, respectively (Figure 2b), and the electron pitch angle distribution (PAD, Figure 2d) show an interesting evolution across the boundary, similar to other diffusion region events observed by MMS [*Lavraud et al.*, 2016]. The crossing of the MSH separatrix is
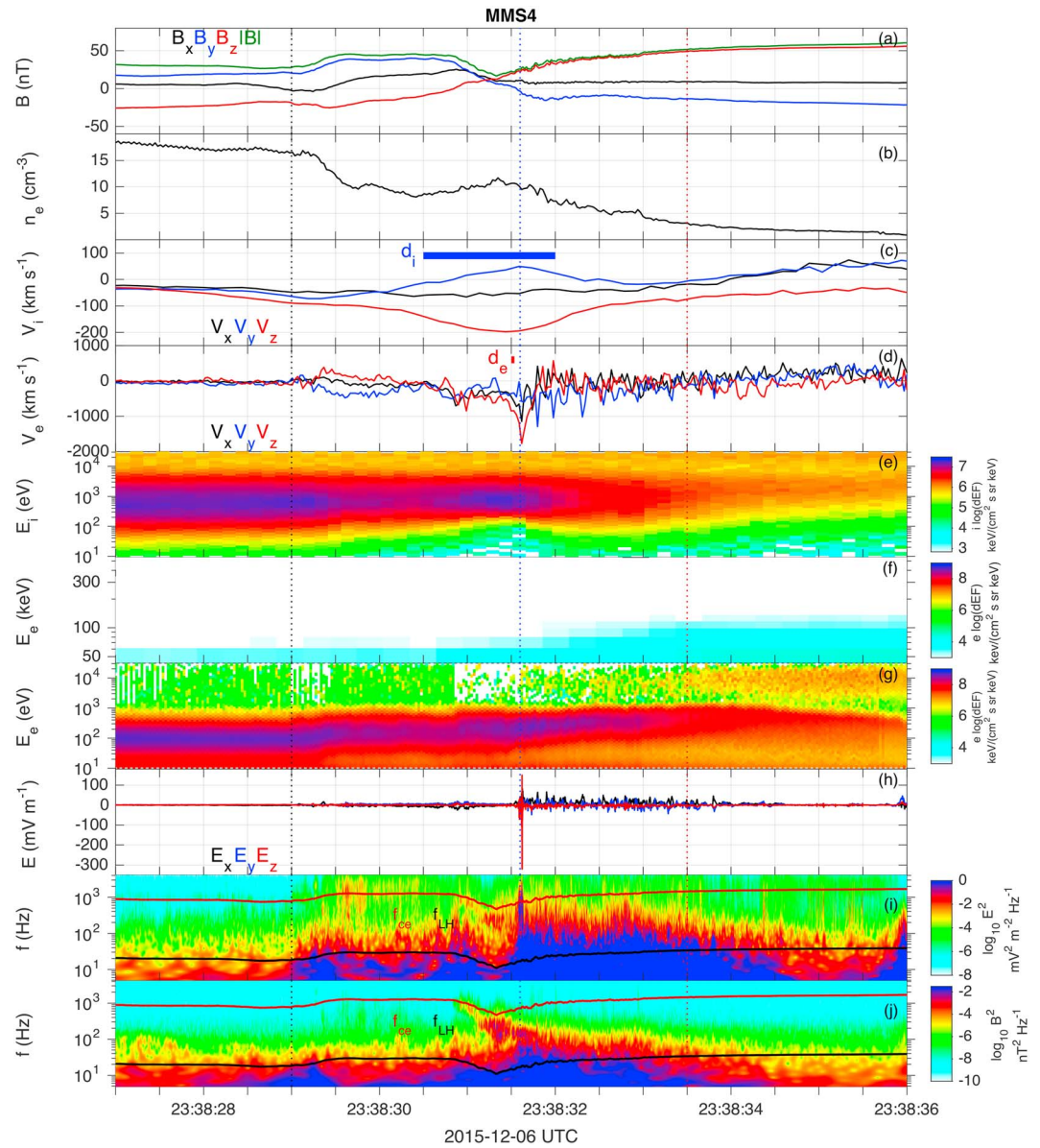
Figure 1. Overview of the magnetopause crossing observed by MMS4 on 6 December 2015 in GSE coordinates. (a) **B**. (b) n_e. (c) **V**$_i$. (d) **V**$_e$. (e) Omnidirectional ion differential energy flux. (f, g) Omnidirectional electron differential energy flux. (h) **E**. (i) Spectrogram of **E**. (j) Spectrogram of **B**. The black, blue, and red vertical dotted lines indicate the MSH separatrix, electron jet, and MSP electron edge, respectively.

associated with an increase of $T_{e\perp}$, and the electron distribution function becomes approximately isotropic. Entry into the central part of the CS at 23:38:31.0 UT is associated with another increase in $T_{e\perp}$. A region with anisotropy factor $\alpha_e = T_{e\parallel}/T_{e\perp} \simeq 0.5$ is observed until 23:38:31.6 UT (location of the fast electron jet and strong E fields). The PAD, Figure 2d, has a maximum at 90°. Such electron anisotropy is expected in the outflow region 1–2 d_i away from the X line [*Pritchett and Mozer*, 2009]. In this region we also observe electromagnetic waves starting just below the electron cyclotron frequency f_{ce} and drifting down in frequency, Figure 1j. These waves are right-hand circularly polarized (not shown) and thus are whistler waves. Such localized whistlers can be indicative of local pileup of the magnetic field, leading to betatron heating of electrons (increase of $T_{e\perp}$) and generation of whistlers due to temperature anisotropy $T_{e\perp} > T_{e\parallel}$ [*Khotyaintsev et al.*, 2011; *Viberg et al.*, 2014].

At the peak of the fast electron jet at 23:38:31.6 UT α_e changes drastically due to an increase in $T_{e\parallel}$, reaching $\alpha_e \sim 3$ within 2 s. If we exclude the PLS population ($E > 2$ keV, Figure 2c), the maximum value of α_e is ~ 7.
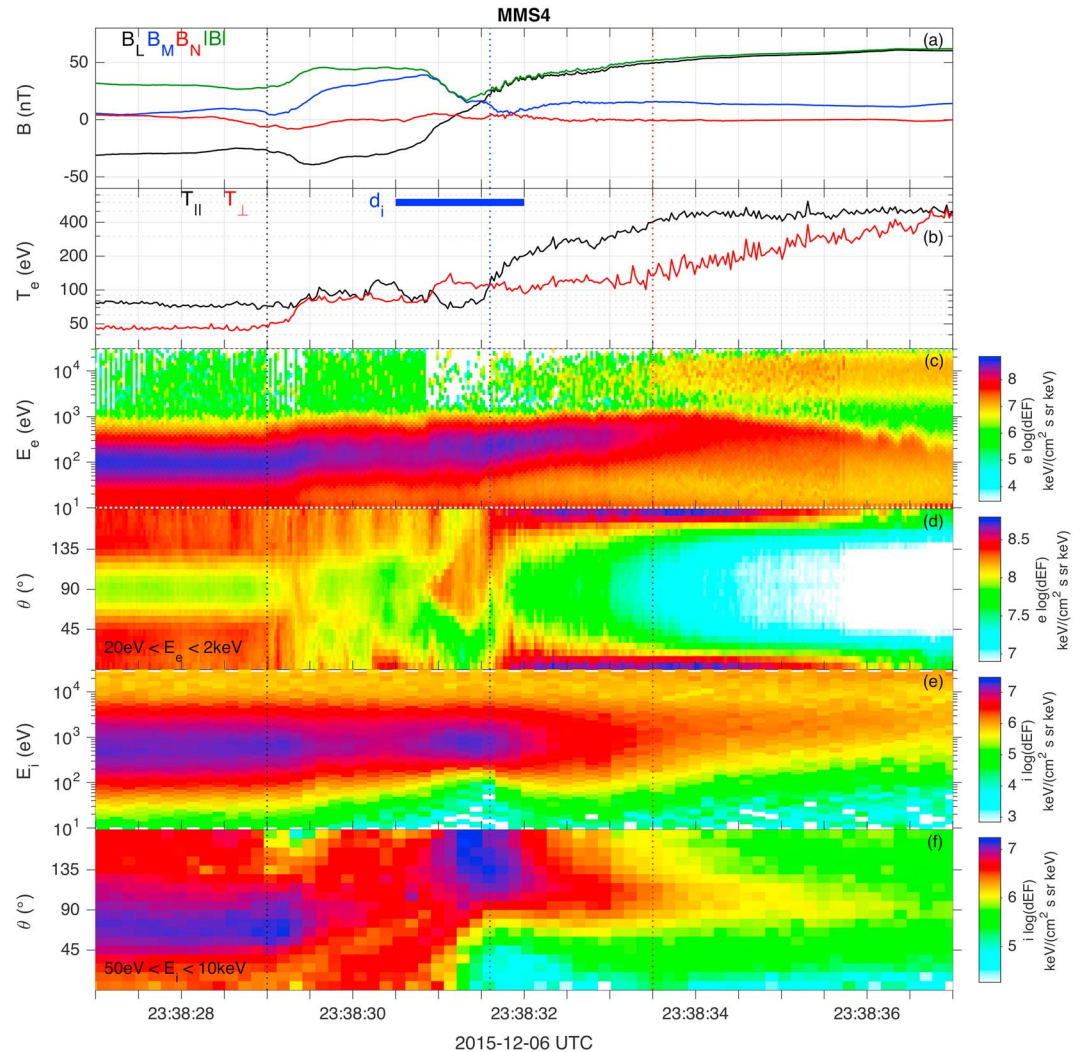
Figure 2. Pitch angle distributions of electrons and ions at the magnetopause crossing observed by MMS4. (a) **B** in LNM coordinates. (b) Parallel and perpendicular electron temperatures. (c) Omnidirectional electron differential energy flux. (d) Electron pitch angle distributions for the energy ranges $20\,eV < E_e < 2\,keV$. (e) Omnidirectional ion differential energy flux. (f) Ion pitch angle distributions for the energy range $50\,eV < E_e < 10\,keV$. The black, blue, and red vertical dotted lines indicate the MSH separatrix, electron jet, and MSP electron edge, respectively.

The large α_e corresponds to counterstreaming electron populations at pitch angles 0° and 180° (Figure 2d). Such a strong anisotropy in the inflow region is only expected very close to the X line [*Egedal et al.*, 2011].

Figure 2f shows the ion PAD. In the MSP inflow region the ions have pitch angles close to 90°, while within the jet the distribution is spread between 90° and 180°. The 90° ions in the MSP inflow region can be explained by a finite gyroradius effect, which indicates that the scale of the inflow region with strong $T_{e\parallel}$ is of the order of $\rho_i \simeq 130$ km (for 2 keV ions), where ρ_i is the ion gyroradius. The observed MSP side of the boundary is clearly different from a usual layered structure with the ion edge being closer to the CS and the electron edge (and the separatrix) located deeper in the magnetosphere [*Lindstedt et al.*, 2009; *Øieroset et al.*, 2015]. Such a finite gyroradius effect is only expected in close proximity to the X line; at larger distances we first expect to see the field-aligned ions when approaching the MP from the MSP side [*Khotyaintsev et al.*, 2004].

Next we investigate the ion and electron perpendicular velocities and compare them to the convection velocity, $\mathbf{V}_\perp = \mathbf{E} \times \mathbf{B}/|\mathbf{B}|^2$ (Figure 3). One can clearly see that the ion and electron motions are decoupled, i.e. $\mathbf{V}_{i\perp} \neq \mathbf{V}_{e\perp} \simeq \mathbf{V}_\perp$, in particular at $B_L \sim 0$. Such behavior confirms the narrow kinetic scale of the CS and close proximity to the X line. Decoupling of ion and electron motions within the CS is a clear signature of the ion diffusion region.
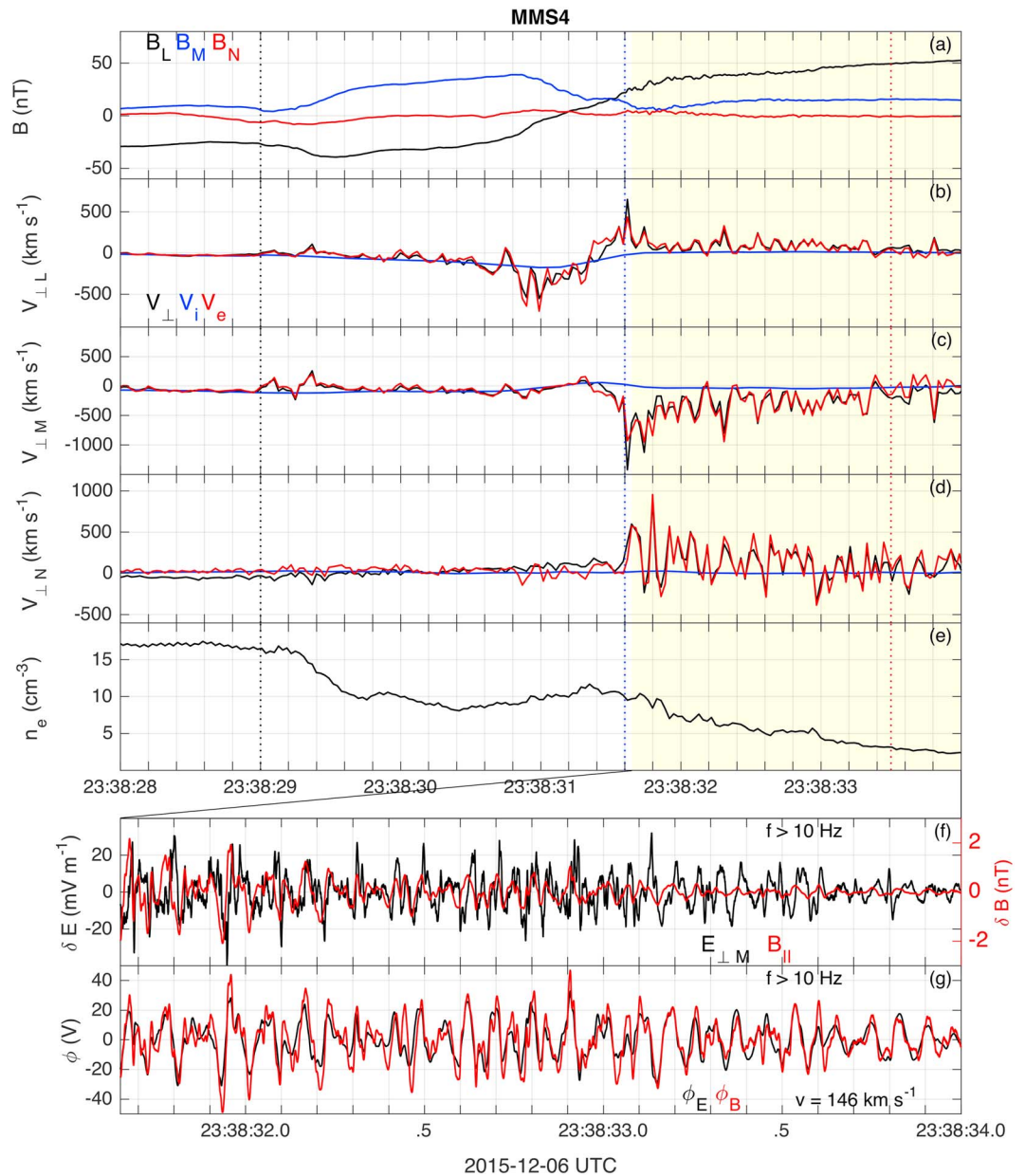
Figure 3. Comparison of the convection velocity $\mathbf{V}_\perp$ and perpendicular velocities of ions and electrons, $\mathbf{V}_{i\perp}$ and $\mathbf{V}_{e\perp}$, observed by MMS4 in LNM coordinates. (a) $\mathbf{B}$. (b–d) $\mathbf{V}_\perp$, $\mathbf{V}_{i\perp}$, and $\mathbf{V}_{e\perp}$ along the L, M, and N directions, respectively. (e) n_e. The black, blue, and red vertical dotted lines indicate the MSH separatrix, electron jet, and MSP electron edge, respectively. (f and g) The properties of the lower hybrid drift waves with frequencies $f > 10$ Hz observed in the yellow shaded region of Figures 3a–3e. Wave fields $\delta\mathbf{E}_{\perp M}$ and $\delta\mathbf{B}_\parallel$ (Figures 3f) and potentials ϕ_E and ϕ_B (Figures 3g).

The rapid fluctuations on the MSP side of the CS (the yellow shaded region of Figures 3a–3e) are related to the lower hybrid drift instability (LHDI) at the density gradient [*Norgren et al.*, 2012]. As expected at lower hybrid time scales, the ions are demagnetized, while the electrons are $\mathbf{E} \times \mathbf{B}$ drifting, which is confirmed by the excellent agreement between $\mathbf{V}_{e\perp}$ and $\mathbf{V}_\perp$. Figures 3f and 3g show the properties of the lower hybrid drift waves (high-pass filtered at frequencies $f > 10$ Hz; f_{LH} is plotted in Figures 1i and 1j). Figure 3f shows the perpendicular electric field fluctuations in the M direction, $\delta\mathbf{E}_{\perp M}$, and the fluctuation magnetic field parallel to $\mathbf{B}$, $\delta\mathbf{B}_\parallel$. Both the parallel and perpendicular components of $\delta\mathbf{B}$ increase as n_e increases and $|\mathbf{B}|$ decreases, or equivalently as the plasma β increases, indicating that the lower hybrid drift waves become more electromagnetic toward the CS center. Figure 3g shows the wave potential $\phi_B = (B_0/n_e e \mu_0)\delta\mathbf{B}_\parallel$, which peaks at ≈ 50 V.
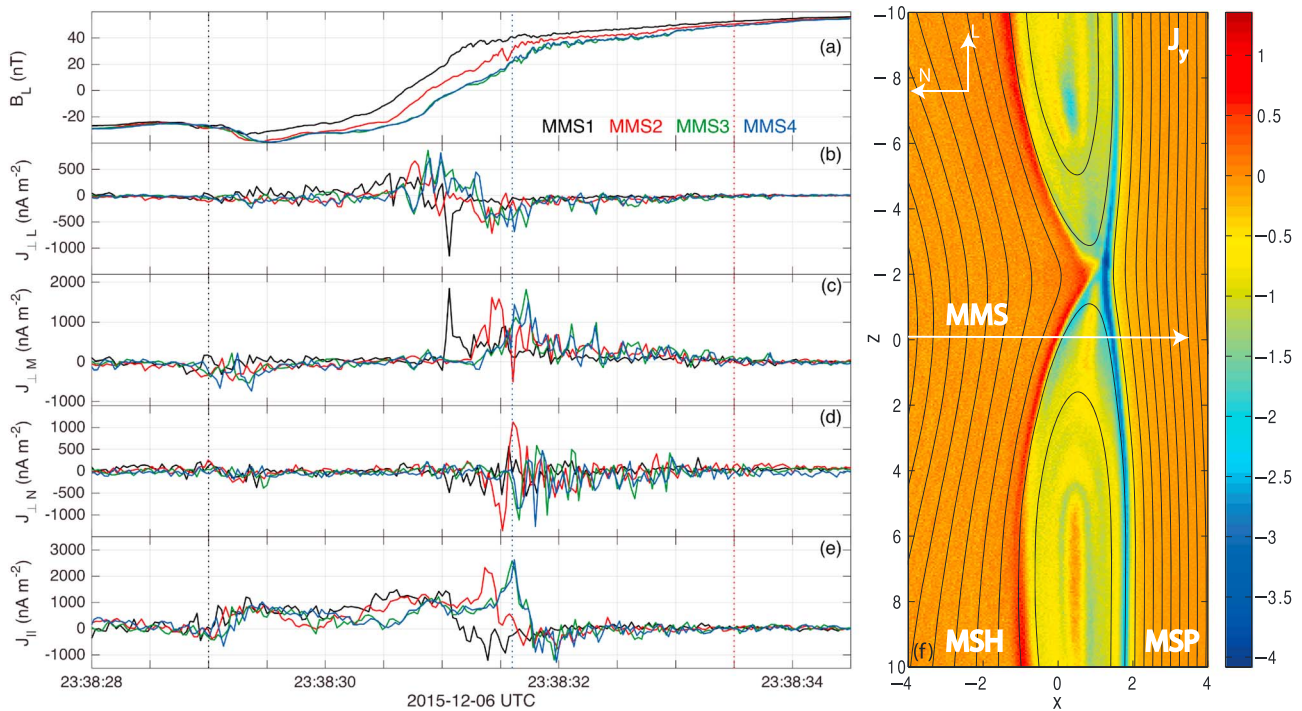
Figure 4. Perpendicular and parallel current densities **J** computed from the particle moments for each spacecraft. (a) B_L. (b–e) $J_{\perp L}$, $J_{\perp M}$, $J_{\perp N}$, and $J_{\parallel}$, respectively. In each panel the black, red, green, and blue curves are for MMS1, MMS2, MMS3, and MMS4, respectively. The black, blue, and red vertical dotted lines indicate the MSH separatrix, electron jet, and MSP electron edge, respectively. (f) J_y (corresponding to J_M) in the units of Jy/en_0V_A from 2-D PIC simulations [*Pritchett and Mozer*, 2009] and an expected path of MMS across the reconnection region. The spatial dimensions are in units of the ion inertial length, d_i.

The phase velocity **v** of the lower hybrid drift waves is found by fitting $\phi_E = \int \delta \mathbf{E} dt \cdot \mathbf{v}$ to ϕ_B (see *Norgren et al.* [2012] for details of the fitting procedure). The best fit of ϕ_E to ϕ_B (shown in Figure 3g, correlation coefficient 0.82) yields $\mathbf{v} = 146 \times [0.29, -0.90, 0.31]$ km s^{-1} (LNM), indicating that the waves propagate along the magnetopause plane, approximately in the $-M$ direction. The excellent agreement between ϕ_E and ϕ_B over this region suggests that **v** does not change significantly, although δ**B** increases toward the magnetopause. We estimate the wavelength to be $\lambda \sim 15$ km, corresponding to a wave number $k \approx 4.2 \times 10^{-4}$ m^{-1}, or equivalently $k\rho_e \approx 0.2$–0.6, where ρ_e is the electron thermal gyroradius. We observe similar lower hybrid drift waves on each spacecraft at the magnetopause crossing.

Figure 4 shows the evolution of current density **J** seen by each spacecraft throughout the ion diffusion region. We plot $\mathbf{J} = q_e n_e(\mathbf{V}_i - \mathbf{V}_e)$ computed from the particle moments and decompose it into perpendicular and parallel components, $\mathbf{J}_\perp$ and $\mathbf{J}_\parallel$, respectively. We note that excellent agreement is found between **J** computed from curlometer and **J** shown in Figure 4 when averaged from the four spacecraft (not shown). The current is mostly parallel to **B** throughout most of the boundary; we see significant $\mathbf{J}_\perp$ only at the MSP side. $\mathbf{J}_\parallel$ has a peak of ~ 1 µA m^{-2} at the MSH separatrix and a similar but somewhat broader peak of **J** at $B_L \sim 0$. We note that these two peaks have a different time delay between the different spacecraft; the crossing of the B_L reversal is slower than the MSH separatrix. On the MSP side of the B_L reversal we see a narrow region with $\mathbf{J}_\parallel \sim 3$ µA m^2. This CS is clearly seen on all spacecraft, and its timing is consistent with the timing of B_L. Therefore, this is a spatial current structure with a scale at half-maximum of 4 km $= 2.4\,d_e$ (for local $n_e = 10$ cm^{-3}), where $d_e = c/\omega_{pe}$ is the electron inertial length; i.e., it is an electron-scale CS.

Figure 4f shows the out-of-plane current J_Y from a 2-D simulation of asymmetric reconnection by *Pritchett and Mozer* [2009] in the XZ simulation plane (corresponding to the NL plane). The expected MMS trajectory crosses the reconnection region and a narrow electron-scale CS in a vicinity of the X line. Overall, we find good agreement between the observed features and the 2-D simulation, in particular the unipolar out-of-plane Hall magnetic field, density peak at the center of the CS, and ion flow extending to the magnetospheric side of the layer (due to the finite gyroradius effect). The electron-scale current, which is carried predominantly by a field-aligned jet of outflowing electrons, is located at the boundary of electron anisotropy separating $T_{e\perp} > T_{e\parallel}$
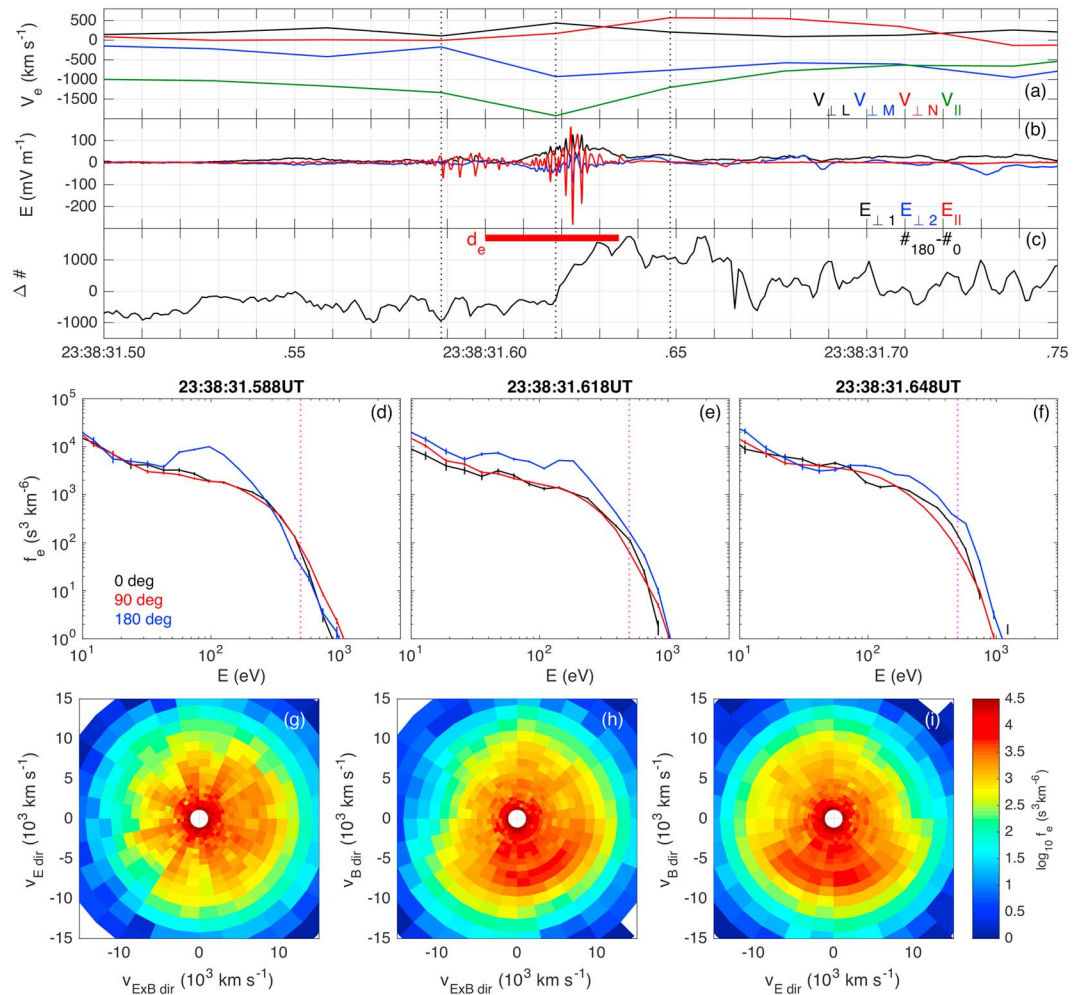
Figure 5. Electrostatic waves and electron distributions associated with the electron jet observed by MMS4. (a) Parallel and perpendicular components of $\mathbf{V}_e$ in LNM coordinates. (b) $\mathbf{E}$ in field-aligned coordinates. (c) Difference in counts, $\Delta\#$, between electrons at $\theta = 0°$ and $180°$ at 500 eV measured by EDI. (d–f) Electron phase-space densities with error bars at pitch angles $\theta = 0°$, $90°$, and $180°$ for the times indicated by the dotted lines in Figures 5a–5c. The dotted magenta lines indicate the energy of electrons measured by EDI. (g–i) Electron distribution at 23:38:31.618 UT (Figure 5e) in the planes (within $\pm 20°$ from the plane) formed by the local $\mathbf{B}$, $\mathbf{E}_\perp$, and $\mathbf{E} \times \mathbf{B}$ directions.

in the center of the CS (flux pileup region) from $T_{e\perp} < T_{e\parallel}$ in the MSP inflow; both types of anisotropies maximize near the X line [*Pritchett and Mozer*, 2009; *Egedal et al.*, 2011]. This suggests that the MSP separatrix, i.e., the field line connected to the X line, must be located at the MSP edge of the electron CS, which implies that we observe intrusion of both the MSH ions and electrons into the MSP inflow region. Such intrusion is an indication of close proximity to the X line and is not observed at larger distances [*Lindstedt et al.*, 2009]. The intruding electrons can be caused by a scattering/diffusion process related to turbulence [*Vaivads et al.*, 2004] or magnetic field curvature [*Lavraud et al.*, 2016]. We note that the observed scale of the MSP electron boundary layer, i.e., the layer located between the electron-scale CS (separatrix) and the MSP electron edge (Figure 2), is $\sim 1 d_i$, which is broader than that in the 2-D simulation (Figure 4f). This discrepancy can be attributed to LHDI which is not present in 2-D. LHDI develops in 3-D at the low-density side of the layer and is driven primarily by the current carried by the ions intruding into the low-density region from the high-density side. This leads to broadening of the separatrix layer, with the LHDI wavelength maximizing close to the X line [*Roytershteyn et al.*, 2012]. Consistent with being close to X line, we observe LHDI with longer wavelength, $k_\perp \rho_e \sim 0.2$–0.6, than typical values $k_\perp \rho_e \sim 1$ [see *Graham et al.*, 2016c]. Thus, a number of features suggest that MMS crossed the reconnection region in close proximity to the X line; comparing to the simulation, we conclude that the crossing is possibly as close as 1–2 d_i from the X line.

The electron-scale CS corresponds to an electron jet, with peak bulk speed $V_e \approx 2 \times 10^3$ km s^{-1} (Figure 5a), and an electron Mach number $M_e = V_e/v_{Te\perp} = 0.35$, where $v_{Te\perp}$ is the perpendicular electron thermal speed. The jet is predominantly antiparallel to **B** and also has a significant perpendicular component. Figure 5b shows **E** in field-aligned coordinates, in which a large-amplitude wave in $E_{\parallel}$ is apparent. These electrostatic waves are closely aligned with **B** and peak at ≈ 300 mV m^{-1}. The waves develop when V_e peaks, suggesting that the electron jet is the source of the waves. At this time a large $E_\perp$ is observed ($E_{\perp 1} \sim E_N$), which corresponds to a cross-field potential drop of $\Phi \sim 100$ V across an $\sim d_e$ wide layer. This potential provides an estimate of an upper limit for the parallel potential present within the layer, and it is consistent with the observed energy of the electron beam discussed below.

The electron phase-space densities at pitch angles $\theta = 0°$, 90°, and 180° are shown in Figures 5d–5f, for the three electron distributions closest to the peak V_e (center times of the distributions are indicated by the dotted lines in Figures 5a–5c). Figure 5d shows the electron distribution just prior to the encounter of the most intense waves. A clear beam is seen near pitch angle $\theta = 180°$, corresponding to jet propagating away from the X line. The electron distribution corresponding to the peak V_e (Figures 5e) is characterized by a much broader/higher-temperature electron beam. Based on fits to the observed distributions, the beam density increases between Figures 5d and 5e, resulting in the increase in bulk V_e. The difference in counts between electrons at $\theta = 0°$ and 180° at 500 eV measured by EDI at ~ 1 ms cadence (Figure 5c) shows a sharp increase across the region associated with the strongest waves, indicating rapid changes of the electron distribution. After the intense waves, the electron distribution (Figures 5f) is characterized by a smaller population of electrons propagating away from the X line.

Figures 5g–5i show the distribution at 23:38:31.618 UT (Figure 4e) in the planes formed by the local **B**, $E_\perp$, and **E×B** directions. During a 30 ms accumulation interval of one 3-D distribution, each of the eight FPI-DES detectors (covering 45° in spacecraft azimuth) performs four sequential deflections of the field of view in azimuth [*Pollock et al.*, 2016]. This makes it possible to decompose the distribution into four partial distributions, each of them covering consecutive 7.5 ms intervals corresponding to the four different azimuths. Examining such partial distributions, we find rapid evolution at scales shorter than 30 ms, with an overall tendency for the electron energy to increase with time, consistent with changes in EDI counts at 500 eV, $\Delta\#$ (Figure 5c). Such rapid evolution results in "fingers" separated by $\sim 45°$ in Figure 5g. For $V_e \sim 8 \times 10^3$ km s$^{-1} \sim 180$ eV a crescent-shaped distribution is observed between the $-$**B** and **E×B** directions. At lower V_e an electron population drifting antiparallel to **B** is seen. Overall, this distribution is agyrotropic with the agyrotropy measure $\sqrt{Q} = 0.06$ [*Swisdak*, 2016], as the crescent is centered at an oblique angle from **B**. At the same time the nearby MMS3 observed $\sqrt{Q} = 0.08$. Such a significant agyrotropy and crescent-shaped distribution suggest that the electron jet is observed close to the X line.

The properties of the electrostatic waves can be estimated using interferometry of the axial and spin-plane probes [*Khotyaintsev et al.*, 2010; *Graham et al.*, 2016b]. Based on this method, we estimate the phase speed of the waves to be $v \approx 300$ km s^{-1} antiparallel to **B**, i.e., in the direction of the electron jet. The phase speed is comparable to the local ion thermal speed. Based on v and the observed wave period, we estimate the wavelength λ to be $\lambda \approx 500$ m $\approx 20\,\lambda_D$, where λ_D is the local Debye length. We estimate the maximum potential to be $\phi \approx 20$ V.

The relatively slow phase speed of the waves indicates that the electron jet is unstable to the Buneman instability, even though the observed jet bulk speed, $v_d \approx 2 \times 10^3$ km s^{-1}, is below the Buneman instability threshold, $v_d \sim v_{Te} \sim 5 \times 10^3$ km s^{-1} [*Buneman*, 1959]. However, in a multicomponent plasma with an electron beam and a warm electron background a modified Buneman instability with a lower threshold can develop [*Norgren et al.*, 2015]. We assume that the peak of the beam with $v_d \approx 8 \times 10^3$ km s^{-1} at $\theta = 180°$ in Figure 5e corresponds to the original unstable beam, which is above the Buneman threshold assuming that the beam temperature is $\sim T_{e\perp}$. For the Buneman instability [*Buneman*, 1959] the predicted wavelength is $\sim 2\pi(v_d/v_{Te})\lambda_D \sim 250$ m and the phase speed is $(m_e/2m_i)^{1/3}v_d/2 \sim 0.032v_d \sim 260$ km s^{-1}, which are in good agreement with the observed values. Therefore, we conclude that the waves are likely generated by a Buneman-type instability. The instability will thermalize the electron beam, quickly stabilizing the beam [*Che et al.*, 2013]. This is consistent with the three distributions in Figures 5d–5f, where we first see a clear beam, which finally becomes fully thermalized. The heating time scale [*Che et al.*, 2013], which can be approximated by the cold plasma limit of Buneman growth time $\sim (m_e/2m_i)^{-1/3}f_{pe}^{-1} \sim 1$ ms is sufficiently short to account for the observed rapid evolution of the electron distributions. In addition to electron heating,

the instability couples the electron beam to the ion background, which would dissipate the **J** associated with the electron jet and generate anomalous resistivity. An implication of this is that the narrow electron jet observed here can only develop near the X line before electrostatic instabilities thermalize the drifting electron population.

3. Conclusions

We presented MMS observations of an electron-scale current sheet and electron outflow jet for asymmetric reconnection with a weak guide field near the subsolar magnetopause. A number of factors indicate that MMS crossed the reconnection region in close proximity to the X line, possibly as close as $1-2$ d_i: narrow kinetic-scale $\sim d_i$ ion jet, decoupling of electron and ion motions within the layer, localized electron temperature anisotropy with $T_{e\perp}>T_{e\parallel}$ and associated whistler waves, strong electron temperature anisotropy $T_{e\parallel}/T_{e\perp}\sim 7$ (for energies below 2 keV), and magnetosheath ions with 90° pitch angle in the magnetospheric inflow region (low-density side). Also, comparison with 2-D particle-in-cell (PIC) simulations [*Pritchett and Mozer*, 2009] shows excellent agreement with the observed signatures and indicates close proximity to the X line. We observe large-amplitude LHDI turbulence with wave potentials $\sim kT_e$ within a separatrix region on the low-density side of the magnetopause. The observed thickness of the region is significantly larger than obtained in the 2-D simulations [*Pritchett and Mozer*, 2009], which suggests that LHDI turbulence can be responsible for broadening the layer, as found in 3-D simulations [*Roytershteyn et al.*, 2012].

The electron jet observed within the reconnection region has a Mach number of 0.35 and is associated with increased electron agyrotropy reaching up to $\sqrt{Q}=0.06-0.08$. The electron outflow jet is unstable to a Buneman-type instability and leads to the generation of intense electrostatic waves with $E_\parallel$ reaching 300 mV m^{-1}. We see evidence of strong interaction between the large-amplitude waves and the electron beam, leading to quick thermalization of the beam and stabilization of the instability. This provides a mechanism for electron heating and braking of the electron flow due to electron-ion drag, and thus, such electrostatic instability introduces resistivity. Our observations demonstrate that electrostatic turbulence plays an important role in the electron-scale physics of asymmetric reconnection with a guide field.

References

Blake, J. B., et al. (2015), The Fly's Eye Energetic Particle Spectrometer (FEEPS) Sensors for the Magnetospheric Multiscale (MMS) Mission, *Space Sci. Rev.*, *199*, 309–329, doi:10.1007/s11214-015-0163-x.

Buneman, O. (1959), Dissipation of currents in ionized media, *Phys. Rev.*, *115*, 503–517, doi:10.1103/PhysRev.115.503.

Burch, J. L., T. E. Moore, R. B. Torbert, and B. L. Giles (2015), Magnetospheric multiscale overview and science objectives, *Space Sci. Rev.*, *199*, 5–21, doi:10.1007/s11214-015-0164-9.

Burch, J. L., et al. (2016), Electron-scale measurements of magnetic reconnection in space, *Science*, doi:10.1126/science.aaf2939, in press.

Cassak, P. A., and M. A. Shay (2007), Scaling of asymmetric magnetic reconnection: General theory and collisional simulations, *Phys. Plasmas*, *14*(10), 102,114, doi:10.1063/1.2795630.

Che, H., J. F. Drake, M. Swisdak, and P. H. Yoon (2010), Electron holes and heating in the reconnection dissipation region, *Geophys. Res. Lett.*, *37*, L11105, doi:10.1029/2010GL043608.

Che, H., J. F. Drake, M. Swisdak, and M. L. Goldstein (2013), The adiabatic phase mixing and heating of electrons in Buneman turbulence, *Phys. Plasmas*, *20*(6), 61205, doi:10.1063/1.4811137.

Drake, J. F., M. Swisdak, C. Cattell, M. A. Shay, B. N. Rogers, and A. Zeiler (2003), Formation of electron holes and particle energization during magnetic reconnection, *Science*, *299*, 873–877, doi:10.1126/science.1080333.

Dunlop, M., D. Southwood, K.-H. Glassmeier, and F. Neubauer (1988), Analysis of multipoint magnetometer data, *Adv. Space Res.*, *8*(9), 273–277, doi:10.1016/0273-1177(88)90141-X.

Egedal, J., A. Le, P. L. Pritchett, and W. Daughton (2011), Electron dynamics in two-dimensional asymmetric anti-parallel reconnection, *Phys. Plasmas*, *18*(10), 102901, doi:10.1063/1.3646316.

Ergun, R. E., et al. (2014), The Axial Double Probe and Fields Signal Processing for the MMS Mission, *Space Sci. Rev.*, *199*, 167–188, doi:10.1007/s11214-014-0115-x.

Graham, D. B., Y. V. Khotyaintsev, A. Vaivads, M. André, and A. N. Fazakerley (2014), Electron dynamics in the diffusion region of an asymmetric magnetic reconnection, *Phys. Rev. Lett.*, *112*, 215004, doi:10.1103/PhysRevLett.112.215004.

Graham, D. B., Y. V. Khotyaintsev, A. Vaivads, and M. André (2015), Electrostatic solitary waves with distinct speeds associated with asymmetric reconnection, *Geophys. Res. Lett.*, *42*, 215–224, doi:10.1002/2014GL062538.

Graham, D. B., A. Vaivads, Y. V. Khotyaintsev, and M. André (2016a), Whistler emission in the separatrix regions of asymmetric magnetic reconnection, *J. Geophys. Res. Space Physics*, *121*, 1934–1954, doi:10.1002/2015JA021239.

Graham, D. B., Y. V. Khotyaintsev, A. Vaivads, and M. André (2016b), Electrostatic solitary waves and electrostatic waves at the magnetopause, *J. Geophys. Res. Space Physics*, *121*, 3069–3092, doi:10.1002/2015JA021527.

Graham, D. B., et al. (2016c), Electron currents and heating in the ion diffusion region of asymmetric reconnection, *Geophys. Res. Lett.*, *43*, doi:10.1002/2016GL068613, in press.

Jara-Almonte, J., W. Daughton, and H. Ji (2014), Debye scale turbulence within the electron diffusion layer during magnetic reconnection, *Phys. Plasmas*, *21*(3), 32114, doi:10.1063/1.4867868.

Khotyaintsev, Y., S. Buchert, K. Stasiewicz, A. Vaivads, S. Savin, V. O. Papitashvili, C. J. Farrugia, B. Popielawska, and Y.-K. Tung (2004), Transient reconnection in the cusp during strongly negative IMF B_y, *J. Geophys. Res.*, *109*, 4204, doi:10.1029/2003JA009908.

Khotyaintsev, Y. V., A. Vaivads, A. Retinò, M. André, C. J. Owen, and H. Nilsson (2006), Formation of inner structure of a reconnection separatrix region, *Phys. Rev. Lett.*, *97*, 205003, doi:10.1103/PhysRevLett.97.205003.

Khotyaintsev, Y. V., A. Vaivads, M. André, M. Fujimoto, A. Retinò, and C. J. Owen (2010), Observations of slow electron holes at a magnetic reconnection site, *Phys. Rev. Lett.*, *105*, 165002, doi:10.1103/PhysRevLett.105.165002.

Khotyaintsev, Y. V., C. M. Cully, A. Vaivads, M. André, and C. J. Owen (2011), Plasma jet braking: Energy dissipation and nonadiabatic electrons, *Phys. Rev. Lett.*, *165001*(16), doi:10.1103/PhysRevLett.106.165001.

Lavraud, B., et al. (2016), Currents and associated electron scattering and bouncing near the diffusion region at Earth's magnetopause, *Geophys. Res. Lett.*, *43*, 3042–3050, doi:10.1002/2016GL068359.

Le Contel, O., et al. (2014), The search-coil magnetometer for MMS, *Space Sci. Rev.*, *199*, 257–282, doi:10.1007/s11214-014-0096-9.

Lindqvist, P.-A., et al. (2014), The spin-plane double probe electric field instrument for MMS, *Space Sci. Rev.*, *199*, 137–165, doi:10.1007/s11214-014-0116-9.

Lindstedt, T., Y. V. Khotyaintsev, A. Vaivads, M. André, R. C. Fear, B. Lavraud, S. Haaland, and C. J. Owen (2009), Separatrix regions of magnetic reconnection at the magnetopause, *Ann. Geophys.*, *27*, 4039–4056.

Murphy, N. A., M. P. Miralles, C. L. Pope, J. C. Raymond, H. D. Winter, K. K. Reeves, D. B. Seaton, A. A. van Ballegooijen, and J. Lin (2012), Asymmetric magnetic reconnection in solar flare and coronal mass ejection current sheets, *Astrophys. J.*, *751*, 56, doi:10.1088/0004-637X/751/1/56.

Norgren, C., A. Vaivads, Y. V. Khotyaintsev, and M. André (2012), Lower hybrid drift waves: Space observations, *Phys. Rev. Lett.*, *109*(5), 55001, doi:10.1103/PhysRevLett.109.055001.

Norgren, C., M. André, D. B. Graham, Y. V. Khotyaintsev, and A. Vaivads (2015), Slow electron holes in multicomponent plasmas, *Geophys. Res. Lett.*, *42*, 7264–7272, doi:10.1002/2015GL065390.

Øieroset, M., T. D. Phan, and M. Fujimoto (2004), Wind observations of asymmetric magnetic reconnection in the distant magnetotail, *Geophys. Res. Lett.*, *31*, L12801, doi:10.1029/2004GL019958.

Øieroset, M., T. D. Phan, J. T. Gosling, M. Fujimoto, and V. Angelopoulos (2015), Electron and ion edges and the associated magnetic topology of the reconnecting magnetopause, *J. Geophys. Res. Space Physics*, *120*, 9294–9306, doi:10.1002/2015JA021580.

Pollock, C., et al. (2016), Fast plasma investigation for magnetospheric multiscale, *Space Sci. Rev.*, *199*, 331–406, doi:10.1007/s11214-016-0245-4.

Pritchett, P. L. (2008), Collisionless magnetic reconnection in an asymmetric current sheet, *J. Geophys. Res.*, *113*, A06210, doi:10.1029/2007JA012930.

Pritchett, P. L., and F. S. Mozer (2009), Asymmetric magnetic reconnection in the presence of a guide field, *J. Geophys. Res.*, *114*, A11210, doi:10.1029/2009JA014343.

Retinò, A., et al. (2006), Structure of the separatrix region close to a magnetic reconnection X-line: Cluster observations, *Geophys. Res. Lett.*, *33*, L06101, doi:10.1029/2005GL024650.

Roytershteyn, V., W. Daughton, H. Karimabadi, and F. S. Mozer (2012), Influence of the lower-hybrid drift instability on magnetic reconnection in asymmetric configurations, *Phys. Rev. Lett.*, *108*(18), 185001, doi:10.1103/PhysRevLett.108.185001.

Russell, C. T., et al. (2014), The magnetospheric multiscale magnetometers, *Space Sci. Rev.*, *199*, 189–256, doi:10.1007/s11214-014-0057-3.

Swisdak, M. (2016), Quantifying gyrotropy in magnetic reconnection, *Geophys. Res. Lett.*, *43*, 43–49, doi:10.1002/2015GL066980.

Swisdak, M., B. N. Rogers, J. F. Drake, and M. A. Shay (2003), Diamagnetic suppression of component magnetic reconnection at the magnetopause, *J. Geophys. Res.*, *108*, 1218, doi:10.1029/2002JA009726.

Tanaka, K. G., et al. (2008), Effects on magnetic reconnection of a density asymmetry across the current sheet, *Ann. Geophys.*, *26*, 2471–2483, doi:10.5194/angeo-26-2471-2008.

Torbert, R. B., et al. (2015), The electron drift instrument for MMS, *Space Sci. Rev.*, *199*, 283–305, doi:10.1007/s11214-015-0182-7.

Vaivads, A., M. André, S. C. Buchert, J. Wahlund, A. N. Fazakerley, and N. Cornilleau-Wehrlin (2004), Cluster observations of lower hybrid turbulence within thin layers at the magnetopause, *Geophys. Res. Lett.*, *31*, L03804, doi:10.1029/2003GL018142.

Viberg, H., Y. Khotyaintsev, A. Vaivads, M. Andre, and J. Pickett (2013), Mapping HF waves in the reconnection diffusion region, *Geophys. Res. Lett.*, *40*, 1032–1037, doi:10.1002/grl.50227.

Viberg, H., Y. V. Khotyaintsev, A. Vaivads, M. André, H. S. Fu, and N. Cornilleau-Wehrlin (2014), Whistler mode waves at magnetotail dipolarization fronts, *J. Geophys. Res. Space Physics*, *119*, 2605–2611, doi:10.1002/2014JA019892.